

Proceedings of the ASME 2020 15th International Manufacturing Science and Engineering Conference MSEC2020 September 3, 2020, Virtual, Online

MSEC2020-8442

DEFORMATION BEHAVIOR OF GRAINS NEAR DEFECTS IN DIRECT METAL LASER SINTERED INCONEL 718 DURING INDENTATION

Mustafa Rifat, Saurabh Basu*

Harold and Inge Marcus Department of Industrial and Manufacturing Engineering, Penn State University, University Park, PA

ABSTRACT

The present work utilizes Orientation Imaging Microscopy and Finite Element Modelling to analyse microstructure evolution in grains near defects during plane strain indentation of direct metal laser sintered Inconel 718. Defects are inevitably produced during printing of metals and they degrade the mechanical behaviour of parent components. Understanding microstructure evolution of grains present near defects can help create better predictive models of mechanical behaviour of components resulting from additive manufacturing. In this work, an ex - situ study of microstructure evolution during plane strain indentation of DMLS Inconel 718 specimens is performed. Regions that lie near volumetric porosity defects were studied. Grain Orientation Spread was utilized as a metric to quantify intra - granular deformation. It was seen that microstructure evolution of grains near defects is enhanced due to strain concentrations whereby they exhibit larger orientation spread after plastic deformation. Finite Element Analysis was used to simulate the plane strain indentation test on the specimen in which, porosity defects and roughness textures similar to those seen in the as-received specimen were programmed using the python scripting interface of Abaqus. Results from finite element analysis were compared with insights from microstructure analysis to describe evolution of microstructure during deformation near defects.

Keywords: Direct Metal Laser Sintering; Indentation;]Orientation Imaging Microscopy; Grain Orientation Spread; Porosity; Surface Roughness; Finite Element Analysis

1. INTRODUCTION

Additive Manufacturing (AM) is the process of printing parts in a layer by layer manner, where each layer is fused to its substrate by a localized heat source. This makes AM suitable for building complex geometries that may not be viable using traditional manufacturing routes [1]. For this reason, AM is being adopted in an increasing rate in different sectors such as biomedical [2], aerospace [3], electronic [4], thermal management [5] and prototyping [6]. Unfortunately, there are a few key limitations of AM that make it unsuitable for large scale production. These limitations degrade the performance of components made by AM via microstructure porosity defects and surface texture defects. Several approaches have been devised to address these limitations. They are briefly summarized here:

1.1. Limitations arising from microstructure porosity defects and their mitigation

Fusion of layer with substrate during AM can naturally create porosity defects. The propensity for the formation of such defects increases with the printing speed of AM [7,8] that is characterized as the speed at which the heat source traverses the current layer that is being fused to the substrate. Porosity in additively manufactured components can reduce their ductility and increase the chance of catastrophic stress rupture [9]. These defects also result in stress concentrations in their vicinity, thus encouraging crack growth in fatigue promoting loading conditions and leading to premature failure [10].

Porosity defects in components made by AM are often mitigated by post-processing via hot isostatic pressing (HIP). This process involves heating components at high temperatures and

^{*}Corresponding author: sxb514@psu.edu (Saurabh Basu)

hydrostatic pressures, whereby facing internal walls of porosity are effectively pushed and sealed [11]. HIP is extremely effective at eradicating porosity defects that lie at relatively larger depths from the component surface. However, its efficacy in healing near surface porosity remains debatable. Herein, a standard process in addressing remnant near surface porosity is to remove the skin layer of components resulting from AM by finish machining or super-finishing after HIP is performed, if the geometry permits.

1.2. Limitations arising from surface texture defects and their mitigation

The raw constituent powder used in AM naturally produces rough surface textures during fusion with the relative substrate. Sharp valleys on these textures can act as sites of stress concentration and thereby degrade the mechanical performance of components by enhancing plastic deformation in their vicinity via resulting strain concentrations [12]. The detrimental effects of surface texture valleys can also be enhanced in the presence of nearby porosity defects due to their interaction. Figure 1 schematically illustrates the combined effects of porosity defect and surface roughness in a part.

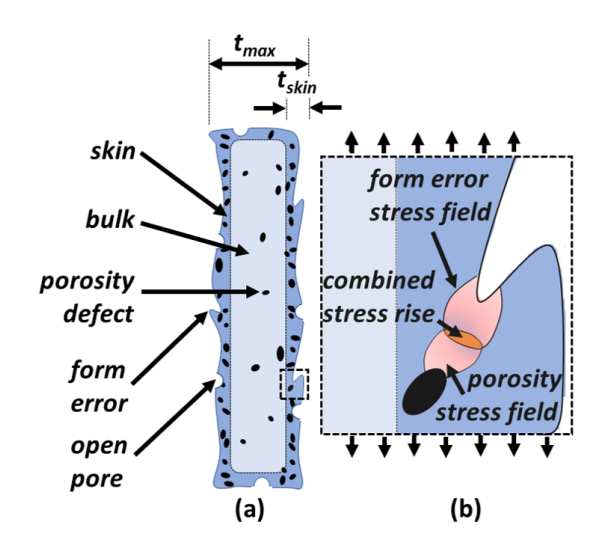


FIGURE 1. (a) SCHEMATIC OF A PART WITH POROSITY AND SURFACE ROUGHNESS; (b) MAGNIFIED VIEW OF THE DASHED BOX IN (a) SHOWING THE EFFECT OF POROSITY DEFECTS AND SURFACE ROUGHNESS WHEN THE PART IS SUBJECTED TO EXTERNAL STRESS

Effects arising from roughness texture are often mitigated by post-processing involving finish machining and non-traditional super finishing operations such as abrasive flow machining and barrel finishing. These operations involve the abrasive action of hard media with the surface of the part created by AM [13, 14]. By controlling parameters such as media shape, size, chemistry, and relative motion, e.g. vibration vs. sliding, ultra-smooth surfaces can be created in parts resulting from AM, thereby rendering them deployable.

The aforementioned defect mitigation approaches entail plastic deformation that is mediated by stress and resulting strain concentrations near porosity defects and surface roughness valleys [15]. From the context of optimizing post-AM processes, it is important to understand the underlying microstructure evolution trajectories. However, most studies that look at effects of porosity defects and surface roughness on response disregard these effects, focusing largely on dynamical aspects. In this article, an ex-situ grain level study of the combined effects of roughness, surficial microstructure and porosity defects on microstructure evolution during shear deformation by plane strain indentation is presented. By utilizing orientation imaging microscopy and finite element analysis, attempt is made to provide an understanding of the effect of porosity on microstructure evolution during shear deformation. In this regard, the present study focuses on the evolution of microstructure in additively manufactured IN718, which is expected to be mediated via coupled effects of roughness and porosity. This study comprises a stepping stone towards delineation of novel plastic deformation phenomena that might exist in additively manufactured microstructures.

The next section (2) introduces grain orientation spread as the chosen tool to quantify the microstructure evolution in grains neighboring porosity or surface roughness defect, section 3 summarizes the materials deformation and microstructure characterization methodology, and finally, section 4 summarizes the results obtained from this methodology and provides an analysis of the results.

2. BACKGROUND-GRAIN ORIENTATION SPREAD

The grain orientation spread (GOS) of a grain is the average value of misorientation between material points within it. GOS is defined as:

$$GOS = \frac{1}{N(N-1)} \sum_{i=1}^{N} \sum_{j=1}^{N} \Delta g(g_i, g_j); i \neq j$$
 (1)

where N is the total number of characterized material points in the grain and g_i , g_j are the orientations of pixels i and j of that grain, respectively. A grain is defined as a zone that is demarcated by a boundary featuring disorientation $< 13^o - 15^o$ with respect to the neighboring material point. The GOS parameter depends on the thermomechanical history of the grain. At pristine, e.g. as-cast conditions, GOS exhibits low values. However, as strain is imposed accumulatively, a grain is subdivided into zones by natural formation of dislocation cells that exhibit

a spread in orientation with respect to each other. This spread increases till a threshold disorientation $\sim 13^o-15^o$ is reached at which point, the parent grain is said to have fragmented to offspring grains. This offspring grain exhibits a low GOS parameter $< 2.6^o$ [16] and with further accumulative straining, this process repeats.

These observations suggest that at least within the limit of low strains that are imposed at ambient temperatures and where grain fragmentation is not observed, the parameter GOS varies monotonically with respect to imposed effective strains. Isothermal deformation up to low strains often takes place during indentation at room temperature at low depths. This allows GOS of a grain to be used as a measure of its deformation during accommodation of global boundary conditions by indentation.

3. EXPERIMENTS

Inconel 718 specimens were additively manufactured using EOS IN 718 powder in EOS M280 DMLS machine. The parameters used in the build are listed in table 1.

After vacuum stress releif, the build was cut off from the baseplate by using wire Electric Discharge Machining (EDM). This wire EDM condition will be referred to as the pristine condition and the wire EDMed specimen will be called pristine specimen in forthcoming sections of the paper.

TABLE 1. PROCESS PARAMETERS USED TO BUILD THE SPECIMEN

Parameter	Value
Laser spot diameter	87.5μm
Layer thickness	$40\mu m$
Preset laser power level	285W
Vacuum stress relief temperature	$1065^o \pm 12^o C$
Vacuum stress relief time	$90\pm15 mins$

Plane strain indentation test was performed on the pristine specimen. To do this, nominally smooth alloy steel dowel pins were acquired from McMaster Carr that exhibited a minimum Rockwell Hardness C52. The speed of indentation was 1mm/min and the maximum depth of indentation (hmax) was 0.09mm. Figure 2a shows the schematic diagram of the experiment with the orientation of the indenter and the build direction. Figure 2b shows a coordinate system (r, θ) - which will be used throughout this article to indicate different portions of the indented cross

section.

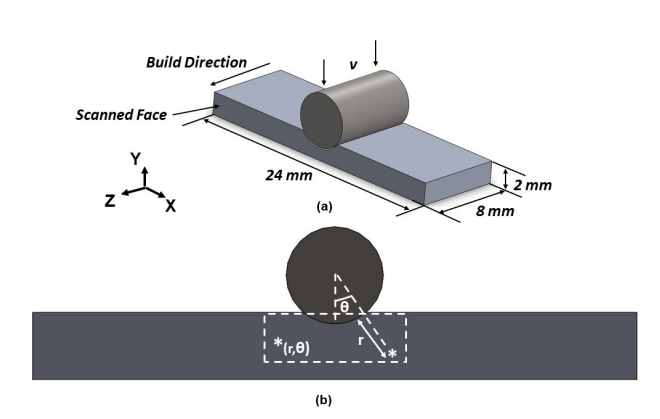


FIGURE 2. (a) SCHEMATIC DIAGRAM OF THE INDENTATION EXPERIMENT; (b) SCHEMATIC DEFINING THE REFERENCE FRAME USED.

Orientation Imaging Microscopy was performed in a Helios 660 SEM equipped with Oxford HKL electron back scattered detector. The characterization was performed at 20KV and 6.4nA. A zone approximately $130\mu m$ deep was scanned with a step size of $0.55\mu m$. Scanning was performed both for the pristine and deformed conditions. AZtec software provided by Oxford Instruments was used to collect the raw scan data. With the help of MATLAB open source library MTEX 5.1.1, different orientation statistics, e.g. GOS were measured. To supplement the characterization of microstructure, implicit plane strain indentation FEA on Abaqus was performed. The workpiece was considered as an isothermal Johnson-Cook material. Parameters used in Johnson-Cook model and mechanical properties of the specimen are listed in table 2.

The indenter was considered as a rigid body. Elements of CPE4 type with element size of $24\mu m$ was chosen. A plane strain thickness of 8mm was assigned for both the workpiece and the indenter. The coefficient of friction selected was 0.64. This was determined in a trial and error basis comparison with different values of coefficient of friction e.g. 0.1, 0.5, 0.64, 0.99 and sticking condition. Furthermore, the surface roughness profile of the pristine specimen was captured by SEM and the same was implemented on the workpiece surface by Python scripting in Abaqus.

TABLE 2. PARAMETERS USED IN JOHNSON-COOK MODEL [17] ALONG WITH THE MECHANICAL PROPERTIES OF THE SPECIMEN

Parameter	Value
A	450 <i>MPa</i>
B	1.7 <i>GPa</i>
n	0.65
m	1.3
T_m	1609 <i>K</i>
Density	$9000kg/m^3$
Elastic Modulus	200 <i>GPa</i>
Poisson Ratio	0.29

4. RESULTS AND DISCUSSION

4.1. Orientation Imaging Microscopy

4.1.1. Pristine Microstructure Orientation Imaging Microscopy of the pristine specimen revealed that there is a gradient in both grain size and aspect ratio with respect to the distance from the surface. The gradient in grain area with respect to the distance from the surface is shown in figure 3a, this indicating small grains in vicinity of the free surface $d \in (0,50\mu m)$, and larger grains at greater distances, $d > 50\mu m$. The area of each grain was calculated by counting the number of pixels within the grain which is defined as the zone demarcated by a boundary featuring disorietation $\theta < 15^{\circ}$. Further, the location of the grain as assumed to be its centroid with respect to the surface.

Figure 3b shows the cross-sectional orientation map characterized parallel to the XY plane, which is perpendicular to the AM build direction shown in Fig. 2a. At the vicinity of the free surface, twins are seen that feature widths $\sim 1-10\mu m$. The parent grains accommodating these twins exhibit mean diameters $\sim 30\mu m$. Beyond depths $d>100\mu m$ from the free surface, columnar grains are seen which are common in materials made by AM due to the epitaxial growth [18].

Figure 3c shows the GOS distribution of grains in the pristine specimen. It can be seen from the distribution that GOS values of the grains in pristine condition ranges in between 0^o-16^o . The distribution is skewed to the right, exhibiting a mean $< GOS >\sim 1.42^o$ and standard deviation of 2.10^o .

4.1.2. Deformed Microstructure Microstructure in the specimen resulting from indentation was characterized in locations $(r, \theta) = (0, 0^o), (0, 5^o), (0, 6.5^o), (0, 8.9^o) and (0, 14^o)$.

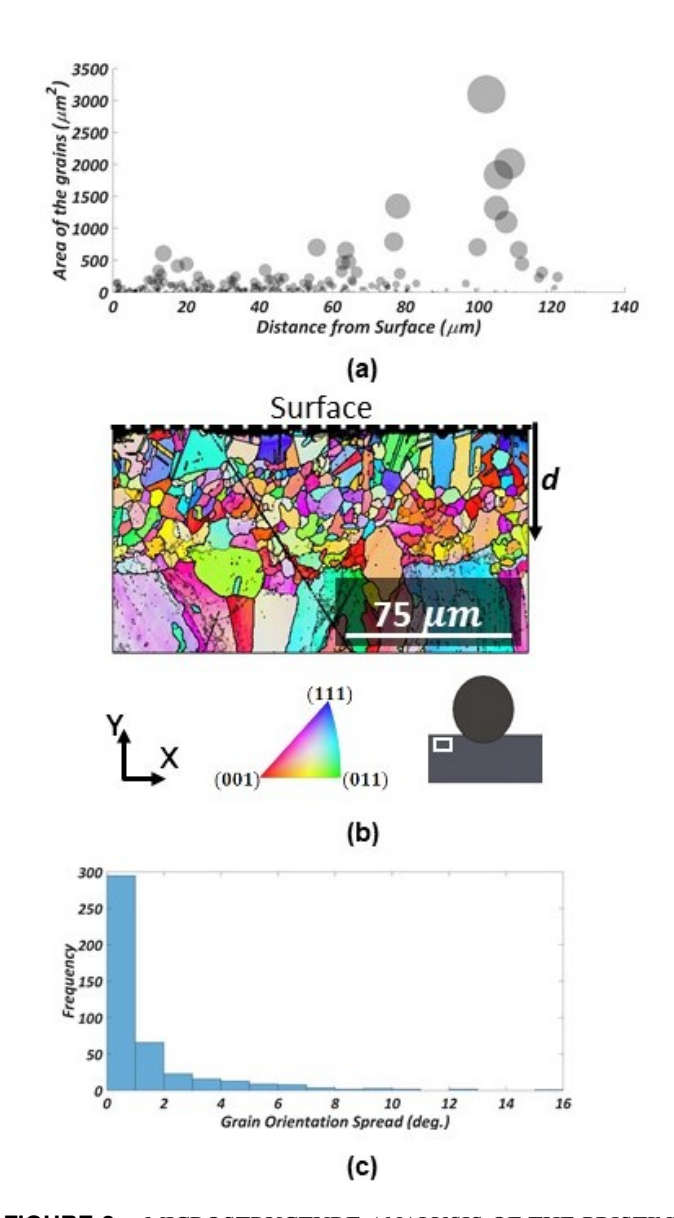


FIGURE 3. MICROSTRUCTURE ANALYSIS OF THE PRISTINE SPECIMEN (a) MEAN GRAIN SIZE WITH RESPECT TO THE DISTANCE FROM SURFACE. (b) ORIENTATION IMAGING MICROSCOPY (THICK BLACK LINES INDICATING HIGH ANGLE GRAIN BOUNDARIES FEATURING DISORIENTATION $\theta > 15^o$ AND THIN BLACK LINES INDICATION LOW ANGLE GRAIN BOUNDARIES $2^o < \theta < 15^o$) (c) GOS DISTRIBUTION EXHIBITED BY THE GRAINS.

The reference system is shown in Fig. 2b. The GOS distributions corresponding to microstructures in these locations are shown in Figs. 4a-4e, respectively. All distributions were found to be skewed to right. The mean and standard deviations of the observed GOS distributions are listed in table 3.

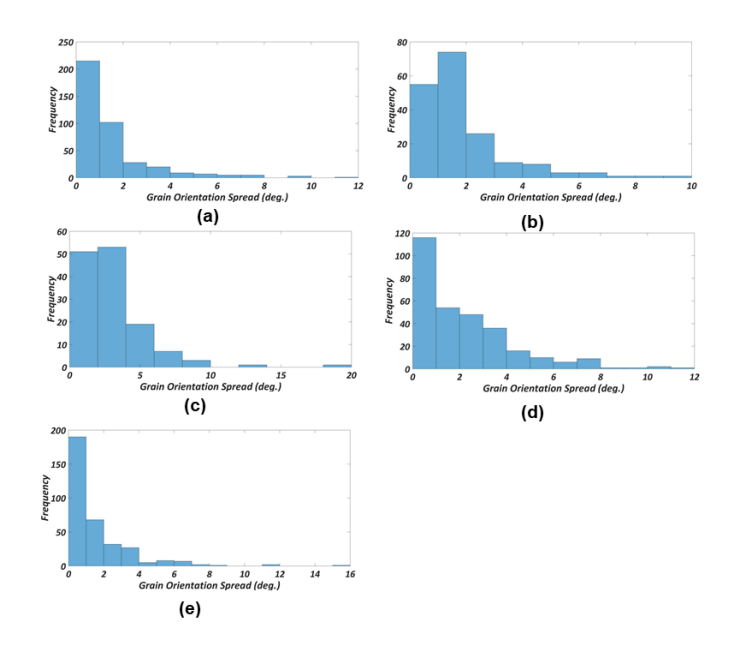


FIGURE 4. GOS DISTRIBUTION OF THE GRAINS (a) $(0,0^o)$; (b) $(0,5^o)$; (c) $(0,6.5^o)$; (d) $(0,8.9^o)$; (e) $(0,14^o)$.

TABLE 3. MEAN AND STANDARD DEVIATIONS OF MISORIENTATION DISTRIBUTIONS EXHIBITED BY MICROSTRUCTURES AT VARIOUS LOCATIONS.

Microstructure	Mean GOS (°)	Standard deviation of GOS (°)
$(0,0^{o})$	1.37	1.75
$(0,5^{o})$	1.80	1.60
$(0,6.5^{o})$	3.04	2.52
$(0, 8.9^{o})$	2.10	2.18
$(0,14^o)$	1.50	1.92

The mean value of GOS was found to be lowest at $(r,\theta)=(0,0^o)$ at GOS=1.37°, directly beneath the indent. It reaches the maximum value of GOS=3.04° degrees at $(0,6.5^o)$ and drops down again at greater angular alignment θ with respect to axis of the indent. The standard deviations of the GOS values are listed in the third column and generally exhibited correlation $R^2\sim 0.7$ with their respective mean values. Such variation in GOS with respect to imposed deformation is prototypical and is often observed during continuous dynamic recrystallization [16].

In order to understand the effect of porosity on microstruc-

ture evolution during plastic deformation, the rest of the article focuses on microstructures in zones $(r, \theta) = (0, 0^o)$ and $(r, \theta) = (0, 8.9^o)$, as shown in Fig. 5a and 5b respectively. These zones exhibited porosity defects, and hence, also exhibit their influence on microstructure evolution during plastic deformation.

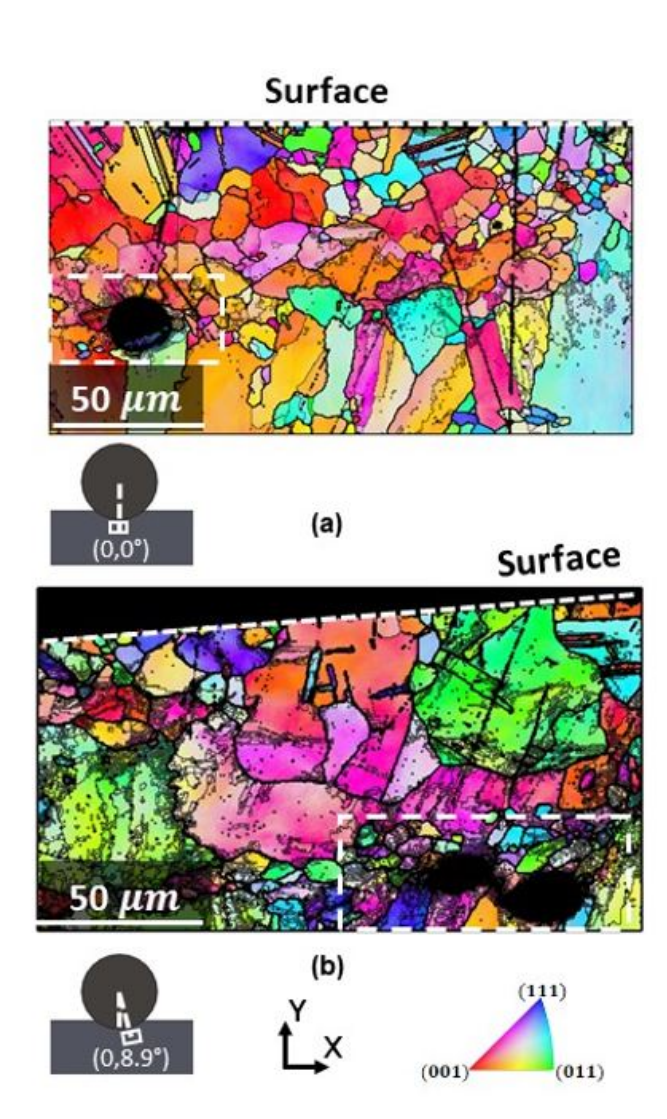


FIGURE 5. MICROSTRUCTURE OF INDENTED SPECIMEN AT LOCATION: (a) $(r,\theta) = (0,0^o)$, (b) $(r,\theta) = (0,8.9^o)$. THICK BLACK LINES INDICATE HIGH ANGLE GRAIN BOUNDARIES FEATURING DISORIENTATION $\theta > 15^o$ AND THIN BLACK LINES INDICATE LOW ANGLE GRAIN BOUNDARIES FEATURING DISORIENTATION $2^o < \theta < 15^o$. THE WHITE BOX IN THE MICROGRAPH SHOWS THE LOCATION OF POROSITY DEFECTS.

Both of the aforementioned microstructures show gradients

in grain size and grain aspect ratio like the pristine specimen. Moderate levels of deformation imposed during indentation are expected to result in moderate changes in microstructures, these dominantly visible in their GOS parameters. For instance, the number average and area weighted GOS of the pristine microstructure was $GOS=1.42^{o}, 3.48^{o}$ respectively. In comparison, microstructures in zones $(r,\theta)=(0,0^{o}),(0,8.9^{o})$ number average and area weighted GOS values of $GOS=1.37^{o}, 4.79^{o}$, and $GOS=2.10^{o}, 5.77^{o}$. This evolution in the microstructure is a consequence of formation of dislocation structures with concomitant spreading of orientation spreads within microstructures in these zones.

However, even simple visual examination of the microstructures suggest that these dislocation structures exhibit heterogeneous densities, higher in zones near porosity defects. Heterogeneity in deformation was delineated by quantifying orientation spreads in grains surrounding the porosity defects. Seven such grains were found in the microstructure characterized at location $(r,\theta)=(0,0^o)$, and twelve such grains were found near the porosity defect in the microstructure in the location $(r,\theta)=(0,8.9^o)$. These grains were labelled a-g and h-s in Figs. 6 and 7, respectively and were demarcated using thick black lines. Orientations spreads of these grains are shown in Tables 4 and 5.

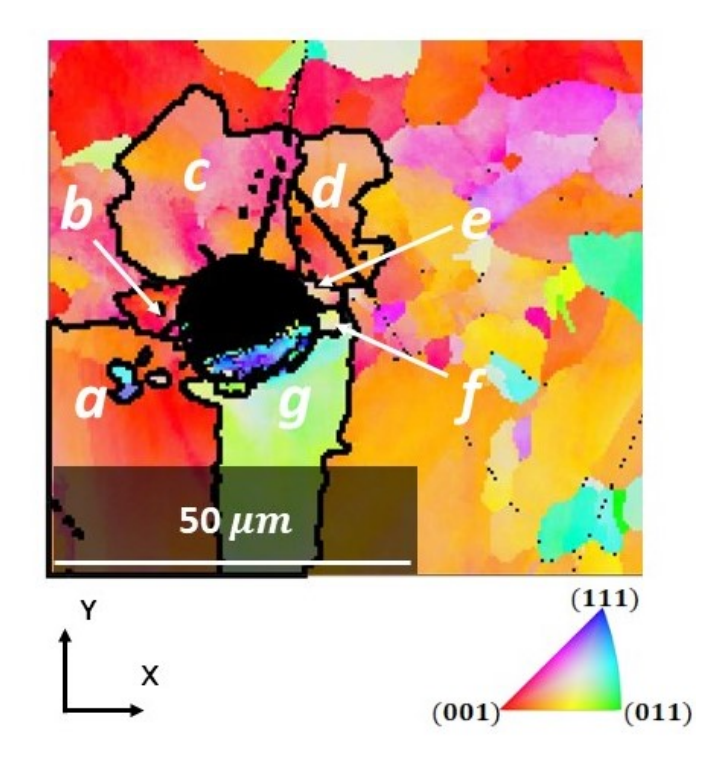


FIGURE 6. SELECTED GRAINS FOR ANALYSIS IN THICK BLACK BORDERS FOR MICROSTRUCTURE $(0,0^o)$

TABLE 4. GOS OF SELECTED GRAINS IN MICROSTRUCTURE $(0,0^{o})$.

Grains	$GOS(^{o})$
а	4.16
b	9.57
c	9.35
d	4.17
e	5.03
f	5.77
g	2.88

All grains in vicinity of porosity defects exhibited GOS parameters greater than number average of the respective GOS distributions, these being GOS=1.37°, and GOS=2.10°, respectively. These results indicate that compared to other grains in the microstructure, grains that lie in close proximity of porosity defects develop higher GOS values after deformation, presumably as a consequence of accommodating greater external strains due to stress concentrations when subjected to external boundary conditions. The variation of GOS characterized with respect to angular position of a grain about a porosity is anisotropic. Grains b and c close to the top left hemisphere of the porosity defects express maximum GOS in location $(r, \theta) = (0, 0^{\circ})$, these being 9.57° and 9.35°, respectively. On the other hand, grain k that lies in the middle of the 2 porosity defects in location $(r, \theta) = (0, 8.9^{\circ})$ expresses maximum GOS=10.13°.

4.2. Finite Element Analysis

In order to delineate the effect of porosity defects in the specimen, plane strain indentation was simulated in ABAQUS. To perform this simulation, the surface roughness profile of the pristine specimen was used in the workpiece to make it as close as possible to the actual sample. Pristine surface profile characterization was done in SEM. The profile was quantified using MATLAB and later was used as an input to ABAQUS python scripting to generate the workpiece surface. Figure 8 shows the SEM image of the surface profile with a length about 1.3mm, average roughness value R_a about $6.5\mu m$ and the maximum distance from the peaks to the valley about $30\mu m$. The distance between consecutive roughness peaks were in the range of $20-400\mu m$. This roughness profile quantified by MATLAB was repeated over the whole specimen surface in ABAQUS.

Apart from the surface roughness profile generation as the

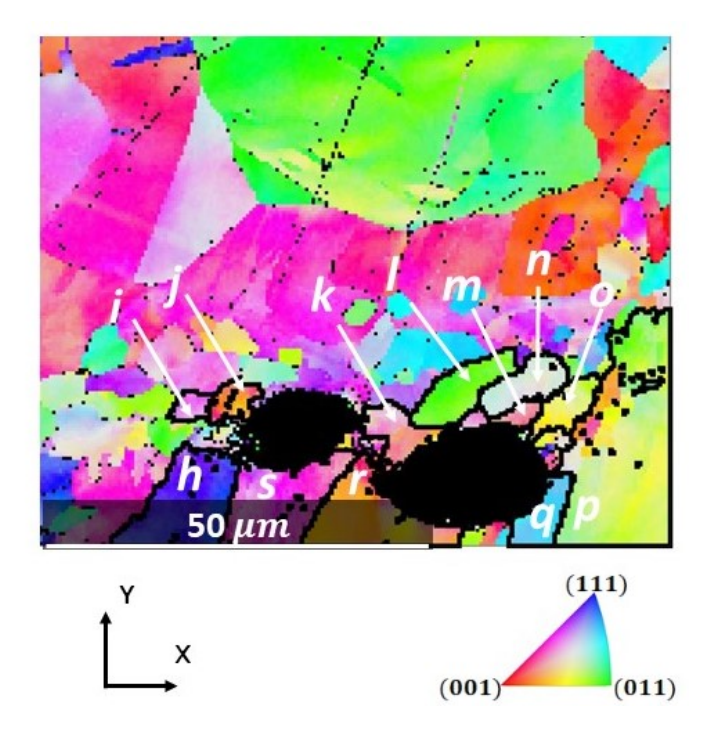


FIGURE 7. SELECTED GRAINS FOR ANALYSIS IN THICK BLACK BORDERS FOR MICROSTRUCTURE $(0, 8.9^{o})$

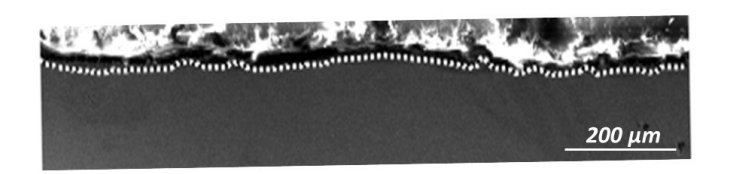


FIGURE 8. SURFACE ROUGHNESS PROFILE CHARACTERIZATION USING SEM- WHITE DOTS ARE THE TRACKS OF THE SURFACE PROFILE

pristine condition, porosity defects were also implanted in the simulation. Circular porosities with uniformly distributed diameter ranging from $30-60\mu m$ were randomly placed inside the workpiece. The defect density was kept about $0.25 defects/mm^2$ as observed in the real specimen. Two pores were intentionally placed at $(r,\theta)=(150\mu m,9^o)$. The location of these two defects were motivated by the two defects present in microstructure $(0,8.9^o)$ as shown in figures 5b inside the white box and magnified in figure 7. Coefficient of friction value of 0.64 was used in the simulation.

Figure 9a and 9b show two instances of the simulation-workpiece with surface roughness as well as porosity and workpiece with only surface roughness respectively. Figure 9c and 9d are the magnified views of the white box in figure 9a and 9b re-

TABLE 5. GOS OF SELECTED GRAINS IN MICROSTRUCTURE $(0, 8.9^{o})$.

Grains	GOS (°)
h	4.60
i	3.15
j	5.86
k	10.13
l	4.11
m	3.25
n	3.45
0	5.86
p	7.41
q	3.40
r	5.35
S	5.23

spectively. The strain field expressed by the numerical specimen comprising only the surface roughness (without porosity defects) exhibit two zones of local strain maxima after indentation, these located on both the sides of the indenter [19]. However, the presence of porosity defects distorts the strain field as shown in figure 9c, where maximum strains were seen in the zone bridging the porosity defect pair. In this regard, it can be expected that the response of grains surrounding the porosity defects will be different than rest of the specimen. This change manifests largest GOS values in grains near the porosity defects as described in the previous section.

5. CONCLUSION

Due to the variation of process parameters during AM process, volumetric defects like porosities are inevitable. These defects have detrimental effects in the resulting mechanical behavior of the part. Understanding the effect of the defects on the mechanical response of AM parts due to loading is of practical importance. In this study, evolution of microstructure after indentation was discussed extensively to understand the behavior of grains surrounding the porosity defects. It was found that the behavior of the grains at the vicinity of the indent and near the porosity defects are different than the overall grain behavior. To be more specific, the GOS of the grains near the surface and surrounding the porosity defects are higher than the overall GOS

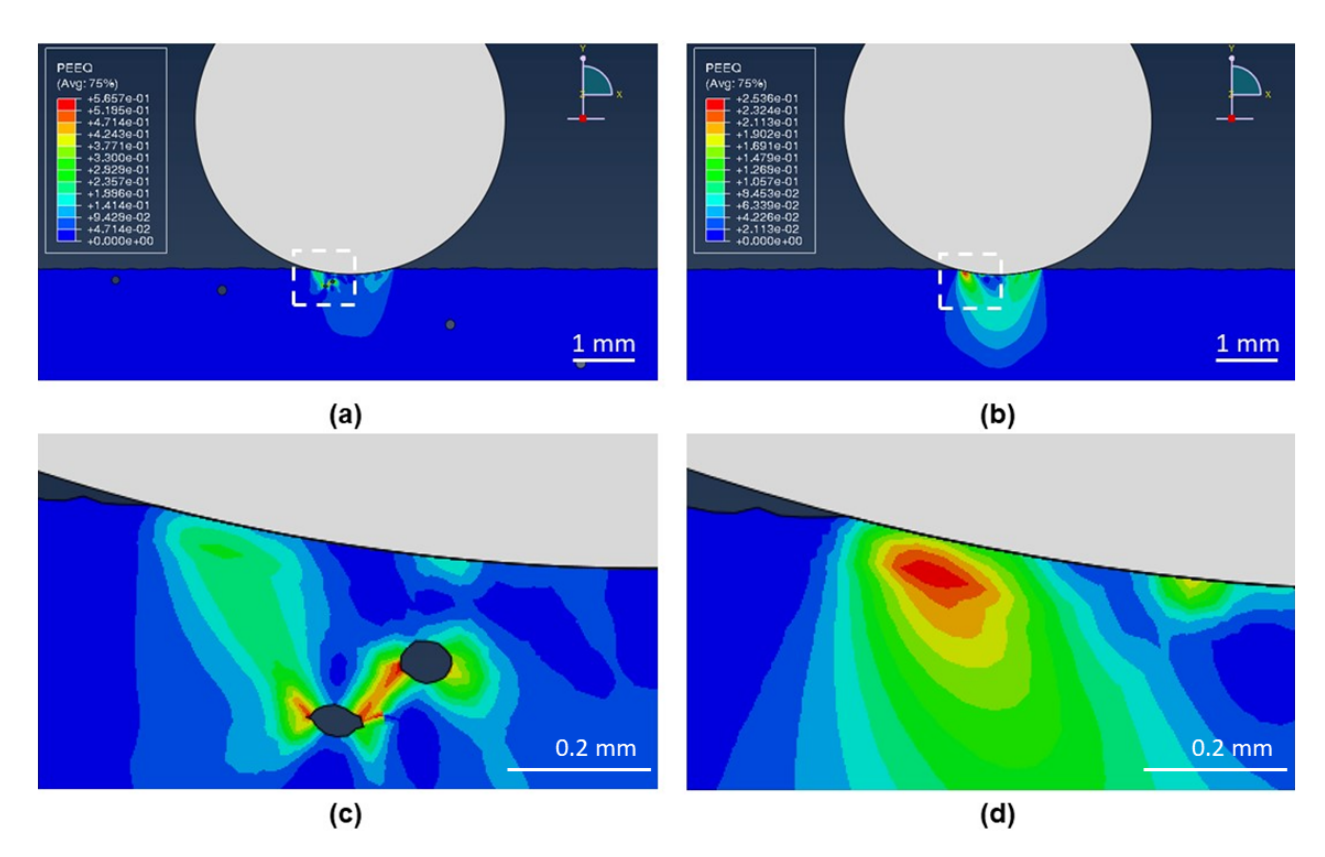


FIGURE 9. EFFECT OF POROSITY DURING THE INDENTATION OF WORKPIECE WITH PRISTINE SURFACE ROUGHNESS CONDITION: (a) EFFECTIVE STRAIN FILED WHEN BOTH SURFACE ROUGHNESS AND POROSITIES ARE PRESENT; (b) EFFECTIVE STRAIN FILED WHEN ONLY SURFACE ROUGHNESS IS PRESENT; (c) AND (d) SHOW MAGNIFIED VIEW OF THE WHITE BOX IN (a) AND (b) RESPECTIVELY

distribution throughout the microstructure. The microstructure analysis was supplemented by FEA of the workpiece having the surface roughness and porosity distribution as the pristine condition. It was seen that zones near the porosities act as a local deformation sinks to accommodate strain imposed during deformation. This result was used to explain the GOS expressed by grains near the defects compared with grains located in other areas of the microstructure.

ACKNOWLEDGMENT

This material is based upon work supported by the National Science Foundation under Grant No. 1825686. Any opinions, findings, and conclusions or recommendations expressed in this material are those of the author(s) and do not necessarily reflect the views of the National Science Foundation.

REFERENCES

- [1] Mueller, B., 2012. "Additive manufacturing technologies—rapid prototyping to direct digital manufacturing". *Assembly Automation*.
- [2] Singh, S., Ramakrishna, S., and Singh, R., 2017. "Material issues in additive manufacturing: A review". *Journal of Manufacturing Processes*, 25, pp. 185–200.
- [3] Schiller, G., 2015. "Additive manufacturing for aerospace". In 2015 IEEE Aerospace Conference, IEEE, pp. 1–8.
- [4] Macdonald, E., Salas, R., Espalin, D., Perez, M., Aguilera, E., Muse, D., and Wicker, R. B., 2014. "3d printing for the rapid prototyping of structural electronics". *IEEE access*, 2, pp. 234–242.
- [5] Norfolk, M., and Johnson, H., 2015. "Solid-state additive manufacturing for heat exchangers". *JOM*, *67*(3), pp. 655–659.
- [6] Lifton, V. A., Lifton, G., and Simon, S., 2014. "Options for additive rapid prototyping methods (3d printing) in mems technology". *Rapid Prototyping Journal*.
- [7] Yasa, E., Deckers, J., and Kruth, J.-P., 2011. "The investigation of the influence of laser re-melting on density, surface

- quality and microstructure of selective laser melting parts". *Rapid Prototyping Journal*.
- [8] Choi, J.-P., Shin, G.-H., Yang, S., Yang, D.-Y., Lee, J.-S., Brochu, M., and Yu, J.-H., 2017. "Densification and microstructural investigation of inconel 718 parts fabricated by selective laser melting". *Powder Technology*, 310, pp. 60–66.
- [9] Zhao, X., Chen, J., Lin, X., and Huang, W., 2008. "Study on microstructure and mechanical properties of laser rapid forming inconel 718". *Materials Science and Engineering: A*, 478(1-2), pp. 119–124.
- [10] Sheridan, L., Scott-Emuakpor, O. E., George, T., and Gockel, J. E., 2018. "Relating porosity to fatigue failure in additively manufactured alloy 718". *Materials Science* and Engineering: A, 727, pp. 170–176.
- [11] Tillmann, W., Schaak, C., Nellesen, J., Schaper, M., Aydinöz, M., and Hoyer, K.-P., 2017. "Hot isostatic pressing of in718 components manufactured by selective laser melting". *Additive Manufacturing*, *13*, pp. 93–102.
- [12] Greitemeier, D., Dalle Donne, C., Syassen, F., Eufinger, J., and Melz, T., 2016. "Effect of surface roughness on fatigue performance of additive manufactured ti–6al–4v". *Materials Science and Technology*, **32**(7), pp. 629–634.
- [13] Wang, X., Fu, Y., and Gao, H., 2016. "Finishing of additively manufactured metal parts by abrasive flow machining". In Proc. 27th Annu. Int. Solid Free. Fabr. Symp., Austin, TX, pp. 2470–2472.
- [14] Boschetto, A., Bottini, L., and Veniali, F., 2018. "Surface roughness and radiusing of ti6al4v selective laser meltingmanufactured parts conditioned by barrel finishing". *The International Journal of Advanced Manufacturing Technol*ogy, 94(5-8), pp. 2773–2790.
- [15] Gao, Y., Yi, J., Lee, P., and Lindley, T., 2004. "The effect of porosity on the fatigue life of cast aluminium-silicon alloys". *Fatigue & Fracture of Engineering Materials & Structures*, **27**(7), pp. 559–570.
- [16] Abolghasem, S., Basu, S., and Shankar, M. R., 2013. "Quantifying the progression of dynamic recrystallization in severe shear deformation at high strain rates". *Journal of Materials Research*, 28(15), pp. 2056–2069.
- [17] Grzesik, W., Niesłony, P., and Laskowski, P., 2017. "Determination of material constitutive laws for inconel 718 superalloy under different strain rates and working temperatures". *Journal of Materials Engineering and Performance*, 26(12), pp. 5705–5714.
- [18] Helmer, H., Bauereiß, A., Singer, R., and Körner, C., 2016. "Grain structure evolution in inconel 718 during selective electron beam melting". *Materials Science and Engineering:* A, 668, pp. 180–187.
- [19] Basu, S., Wang, Z., and Saldana, C., 2016. "Anomalous evolution of microstructure and crystallographic texture during indentation". *Acta Materialia*, *105*, pp. 25–34.